Monthly Notices of the ROYAL ASTRONOMICAL SOCIETY

MNRAS **522,** 693–699 (2023) https://doi.org/10.1093/mnras/stad760
Advance Access publication 2023 March 20

Two new white dwarfs with variable magnetic Balmer emission lines

Joshua S. Reding [1]★ J. J. Hermes [2] J. C. Clemens [1] R. J. Hegedus [1] and B. C. Kaiser [1]

[1]*Department of Physics and Astronomy, University of North Carolina at Chapel Hill, Chapel Hill, NC 27599, USA*
[2]*Department of Astronomy, Boston University, 725 Commonwealth Avenue, Boston, MA 02215, USA*

Accepted 2023 March 6. Received 2023 March 6; in original form 2023 January 5

ABSTRACT

We report the discovery of two apparently isolated stellar remnants that exhibit rotationally modulated magnetic Balmer emission, adding to the emerging DAHe class of white dwarf stars. While the previously discovered members of this class show Zeeman-split triplet emission features corresponding to single magnetic field strengths, these two new objects exhibit significant fluctuations in their apparent magnetic field strengths with variability phase. The Zeeman-split hydrogen emission lines in LP 705−64 broaden from 9.4 to 22.2 MG over an apparent spin period of 72.629 min. Similarly, WD J143019.29−562358.33 varies from 5.8 to 8.9 MG over its apparent 86.394 min rotation period. This brings the DAHe class of white dwarfs to at least five objects, all with effective temperatures within 500 K of 8000 K and masses ranging from 0.65 to 0.83 $M_{\odot}$.

Key words: white dwarfs – stars: individual: LP 705−64; WD J143019.29−562358.33 – stars: magnetic fields – stars: evolution.

1 INTRODUCTION

White dwarf stars are typically photometrically stable objects; 97 per cent of those observed by the late *Kepler* Space Telescope between its original mission and *K2* Campaign 8 are apparently non-variable to within 1 per cent in the *Kepler* filter bandpass (Howell et al. 2014; Hermes et al. 2017b). The remaining 3 per cent host a wide variety of variability mechanisms including pulsations (Warner & Robinson 1972; Winget, van Horn & Hansen 1981), magnetic spots (Maoz, Mazeh & McQuillan 2015), and interactions with binary companions, planets, and planetary debris (Vanderburg et al. 2015; Hallakoun et al. 2018; Vanderbosch et al. 2020). This variable sample provides a means to understand stellar activity and evolution, both intrinsic (e.g. internal structure and dynamics) and extrinsic (e.g. planetary system evolution and interactions with host stars).

Some particularly enigmatic variable white dwarfs stand out from this sample as evading explanation. Among these are the growing class of DAHe white dwarfs: apparently isolated stars whose spectra are characterized by magnetically split (DH) hydrogen Balmer (DA) emission (De), which also exhibit both photometric variability and corresponding time-dependent variations in their Balmer features. The first object discovered in this class was GD 356, and it remained the only member for 35 years (Greenstein & McCarthy 1985). Across these three-and-a-half decades, astronomers studied GD 356 and speculated as to the source of the emission despite there being no apparent companion to feed it.

The prevailing model for most of this time involved a conducting planet orbiting through the stellar magnetosphere, inducing an electromotive force that excites the stellar atmosphere into emission, in a unipolar inductor configuration akin to that which is active in the Jupiter–Io system (Goldreich & Lynden-Bell 1969; Li, Ferrario & Wickramasinghe 1998). It was further proposed that this planet could have formed from material cast off in a double white dwarf merger, similar to how planets are hypothesized to form around millisecond pulsars (Podsiadlowski, Pringle & Rees 1991; Wickramasinghe et al. 2010). However, GD 356 is only a low-amplitude variable ($P_{\rm rot} \approx$ 115 min) due to its rotation axis orientation never moving its emission region fully out of our line of sight, so behaviour exhibited elsewhere on the stellar surface cannot be observed to provide additional information (Brinkworth et al. 2004; Walters et al. 2021).

A second discovery finally established the DAHe class with the identification of SDSS J1252−0234 (Reding et al. 2020), which presents significant (∼5 per cent) photometric variability in SDSS-*g* on a dominant period of 5.3 min. The Balmer features in SDSS J1252−0234 (particularly Hβ) also transition on this photometric period from moderately broadened absorption at photometric maximum to Zeeman-split triplet emission at photometric minimum, which confirms that the emission region is localized on the stellar surface to magnetic spots. The rapid rotation is anomalous compared to typical white dwarf rotation periods of 0.5–2.2 d (Hermes et al. 2017a), which might indicate that the object was formed from a previous stellar merger (Ferrario et al. 1997; Tout et al. 2008; Nordhaus et al. 2011). Gänsicke et al. (2020) then discovered a third object, SDSS J1219+4715, which bears more of a resemblance to GD 356 with its Balmer emission never fully disappearing, but rotates on a slower time-scale ($P \approx 15.3$ h).

In addition to their mysterious behaviour, the DAHe white dwarfs also exhibit a remarkable uniformity in their physical characteristics. All three have masses near the white dwarf population average (0.62 $M_{\odot}$; Genest-Beaulieu & Bergeron 2019), effective temperatures 7500 K $< T_{\rm eff} <$ 8500 K, and mega-gauss magnetic fields ($B_{\rm GD356} = 11$ MG, Greenstein & McCarthy 1985; $B_{\rm J1252} = 5$ MG, Reding et al. 2020; $B_{\rm J1219} = 18$ MG, Gänsicke et al. 2020). This homogeneity and the non-detection of a planetary companion to GD 356 with targeted study suggest that the emission behaviour

★ E-mail: jsreding@unc.edu

may in fact be intrinsic to white dwarfs at this evolutionary phase (Walters et al. 2021). The recent discovery of a similar apparently isolated white dwarf with variable emission, but yet undetectable magnetism, further confounds the nature of this mechanism (SDSS J041246.85+754942.26; Tremblay et al. 2020).

Here, we announce the discovery of two new DAHe white dwarfs, LP 705−64 (*Gaia* $G = 16.9$ mag) and WD J143019.29−562358.33 ($G = 17.4$ mag; henceforth J1430), which each present a unique twist on the established Zeeman-split triplet emission seen in the previous three DAHe. LP 705−64 shows two different emission poles in its spectral variability, with one prominently featuring the classical Zeeman triplet emission at Hα and Hβ like in GD 356, before transitioning to reveal significantly broader Zeeman emission measurable only at Hα. J1430 shows a pole of Zeeman-split triplet absorption in Hβ, which is filled asymmetrically by broader triplet emission half a rotation cycle later, while Hα simultaneously reveals fainter triplet emission across the same transition. Both maintain the other established similarities to the known members of the DAHe class, including in temperature, mass, magnetic field strength, and location in observational Hertzsprung–Russell diagrams.

We describe our survey strategy that uncovered these objects and the corresponding observations in Section 2, and follow with a description of our analysis in Section 3. We then discuss the context and broader implications of these objects, and summarize our conclusions in Section 4.

2 SURVEY STRATEGY AND OBSERVATIONS

2.1 VARINDEX survey and *Gaia* archival data

We discovered the unusual activity in LP 705−64 (*Gaia* DR3 2375576682347401216) and J1430 (*Gaia* DR3 5892465542676716544) using a survey strategy specifically formulated to identify likely DAHe candidates from the broader white dwarf population. We used the *Gaia* DR2 VARINDEX metric, whose calculation is described in Guidry et al. (2021), to identify the most likely variable objects from over 260 000 high-probability white dwarf candidates in *Gaia* DR2 (Gentile Fusillo et al. 2019). Given the physical similarity of the DAHe objects discovered so far, with masses 0.65−0.75 $M_\odot$ and effective temperatures ∼7700 K (Gänsicke et al. 2020), we then limited the selection to the region of the *Gaia* DR2 Hertzsprung–Russell diagram where DAHe white dwarfs are most likely to reside ($12 < M_G < 14$, $0.2 < G_{BP} - G_{RP} < 0.5$; Fig. 1). We then collected identification spectra of the highest VARINDEX objects, and, if there were suggestions of DAHe activity, determined a variability period from archival sources or follow-up photometry, and ultimately collected time-series spectroscopy folded on the variability period to produce a complete chronology of the spectral activity. Details of these observations for LP 705−64 and J1430 are described in the subsections below. Among our first ∼100 survey candidates, LP 705−64 and J1430 are the first two confirmed DAHe; observations of the remaining objects will be detailed in a future manuscript.

LP 705−64 and J1430 have *Gaia* DR2 VARINDEX values of 0.0063 and 0.0131, respectively; this places LP 705−64 near and J1430 well within the top 1 per cent of variable white dwarfs ($\text{VARINDEX}_{DR2} > 0.0074$; Guidry et al. 2021). The parallaxes ϖ for these objects are precise enough and suggest a small enough distance ($d < 0.1$ kpc) such that using $d = 1/\varpi$ should provide a sufficiently accurate estimate of the true distance (Luri et al. 2018). Using this distance value and the updated *Gaia* DR3 proper motions μ_α and μ_δ, we calculate tangential velocity for each object, and find that LP 705−64 has a particularly large v_{tan} that is consistent with <30 per cent of low-mass (0.5–0.75 $M_\odot$) and a vanishingly small fraction of intermediate-mass (0.75–0.95 $M_\odot$) white dwarfs (Wegg & Phinney 2012). We discuss the implications of this further in Section 4. These two objects lack sufficient archival survey photometry in the optical and ultraviolet to perform consistent spectral energy distribution fits for T_{eff} and log g/mass, so we adopt the atmospheric parameters calculated by Gentile Fusillo et al. (2021) using *Gaia* photometry and hydrogen-atmosphere white dwarf models with thick ($M_H/M_{WD} = 10^{-4}$) hydrogen layers (Kowalski & Saumon 2006; Tremblay, Bergeron & Gianninas 2011). This collected information is listed in Table 1. We note that the use of non-magnetic model atmospheres may make photometrically derived effective temperatures and masses artificially low, as magnetism is known to suppress flux particularly in the *Gaia* G_{BP} band, but systematic study suggests this effect is insignificant for stars in the DAHe parameter space (Gentile Fusillo et al. 2018; Hardy, Dufour & Jordan 2023).

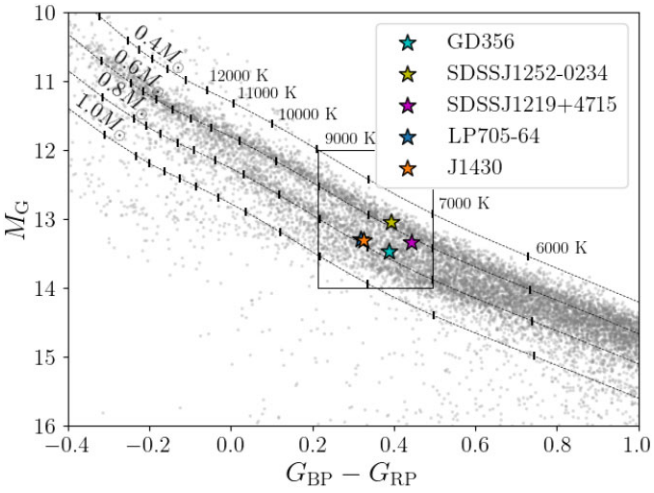

Figure 1. *Gaia* Hertzsprung–Russell diagram of white dwarfs within 100 pc of the Sun in grey along with all DAHe objects discovered to date, VARINDEX survey window, and thick H layer mass tracks from Bédard et al. (2020). LP 705−64 and J1430 have nearly identical locations and maintain the narrow DAHe parameter space.

Table 1. *Gaia* DR3 astrometric parameters and photometry, and estimated T_{eff}, log g, and mass for LP 705−64 and J1430 using H-atmosphere white dwarf models (Kowalski & Saumon 2006; Tremblay et al. 2011; Gentile Fusillo et al. 2021).

Parameter	LP 705−64	J1430
RA (deg, J2016.0)	8.8044	217.5803
Dec. (deg, J2016.0)	−12.4198	−56.3995
ϖ (mas)	18.986 ± 0.088	15.075 ± 0.097
d (pc)	52.67 ± 0.24	66.33 ± 0.43
μ_α (mas yr^{-1})	148.58 ± 0.09	−14.79 ± 0.07
μ_δ (mas yr^{-1})	−150.61 ± 0.08	4.09 ± 0.07
v_{tan} (km s^{-1})	52.89 ± 0.28	4.83 ± 0.06
G	16.888 ± 0.003	17.407 ± 0.003
G_{BP}	16.989 ± 0.011	17.529 ± 0.008
G_{RP}	16.675 ± 0.010	17.220 ± 0.009
P_{WD}	0.993	0.993
T_{eff} (K)	8440 ± 200	8500 ± 170
log g	8.34 ± 0.05	8.37 ± 0.05
Mass ($M_\odot$)	0.81 ± 0.04	0.83 ± 0.03

2.2 SOAR/Goodman HTS identification spectra

Upon sorting our DAHe candidates by VARINDEX, we began collecting identification spectra to detect evidence of spectral activity using the Southern Astrophysical Research (SOAR) 4.1-m telescope and Goodman High-Throughput Spectrograph (HTS) at Cerro Pachón, Chile (Clemens, Crain & Anderson 2004). We acquired three 300-s spectra of J1430 on 2021 April 7 using a 400 line mm^{-1} grating and 3.2 arcsec slit, corresponding to a slit width of 21 Å. Our spectral resolution was therefore limited by the wind-impacted observing conditions at a full width at half-maximum of 17 Å (2.5 arcsec). We bias-subtracted the data and trimmed the overscan regions, then completed reduction using a custom PYTHON routine (Kaiser et al. 2021). We flux-calibrated the spectra using standard star EG 274, wavelength-calibrated using HgAr and Ne lamps, and applied a zero-point wavelength correction using sky lines from each exposure. These spectra, when averaged, showed jagged Balmer features suggestive of activity, and we marked J1430 for time-series follow-up.

Similarly, we collected five 180-s spectra of LP 705−64 on 2021 August 6 using the same grating but with a 1 arcsec (7 Å) slit. Zeeman-split triplet emission features at H α and H β were clearly visible in these single spectra, thereby confirming LP 705−64 as a DAHe.

2.3 *TESS* photometry

The *Transiting Exoplanet Survey Satellite* (*TESS*; Ricker et al. 2015) observed LP 705−64 (TIC 136884288) in Sector 30 with 120-s exposures, collected from 2020 September 23 through 2020 October 19, and J1430 (TIC 1039012860) in Sector 38 with 120-s exposures, collected from 2021 April 29 through 2021 May 26. We extracted these light curves for periodogram analysis using the PYTHON package LIGHTKURVE (Lightkurve Collaboration 2018). The periodograms each show one significant peak, whose corresponding periods ($P_{\rm LP\,705-64} = 36.315$ min and $P_{\rm J1430} = 86.394$ min; Fig. 2) we adopted for planning our time-series spectroscopy. Later analysis revealed nuance in this variability, which we discuss further in Section 3.1.

2.4 SOAR/Goodman HTS time-series spectroscopy

Following our detection of DAHe activity and discernment of photometric variability periods for LP 705−64 and J1430, we returned to SOAR and the Goodman HTS to investigate spectral feature variations corresponding to the photometric variability using time-series spectroscopy. On 2021 July 13, we collected 5.4 h (approximately four presumed variability cycles) of time-series spectra for J1430 in 10-min exposures using the same 400 line mm^{-1} grating and 3.2 arcsec slit as the identification spectra. The spectra were seeing-limited at 1.5 arcsec, and the average overhead for each acquisition was 5.45 s. We performed the same reductions as were used in the SOAR/Goodman HTS identification spectra (Section 2.2).

We targeted LP 705−64 in a similar fashion on 2021 August 30 using 539-s exposures to reflect equal divisions of the apparent *TESS* variability period, accounting for the overhead time between subsequent exposures. We collected 24 exposures in this set across 3.6 h, corresponding to six presumed variability cycles. We discuss folding and combining spectra in these data sets on divisions of the objects' respective variability periods in Section 3.1.

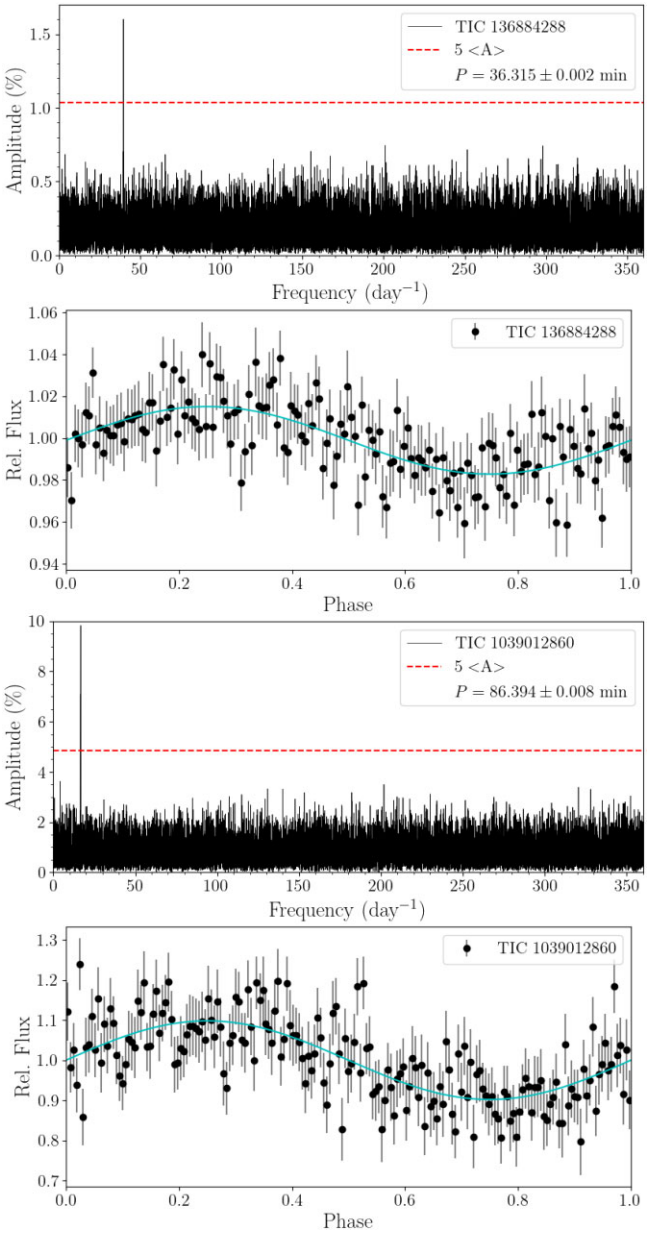

Figure 2. *TESS* periodograms of LP 705−64 (TIC 136884288; top) and J1430 (TIC 1039012860; bottom) with a signficance threshold of five times the periodogram average (Baran & Koen 2021), and phase-folded light curves binned every 100 points. The periodograms suggest dominant photometric periods at $P_{\rm LP705-64} = 36.315$ min and $P_{\rm J1430} = 86.394$ min, respectively, and do not show significant harmonics or additional signals. The likely white dwarf rotation periods are discussed in Section 3.1.

3 ANALYSIS

3.1 Variability and time-series spectroscopy

We performed least-squares fits of a sinusoidal signal $A\sin[2\pi(t/P + \phi)]$ to the LP 705−64 and J1430 *TESS* light curves using the software PERIOD04 (Lenz & Breger 2014), where A is the amplitude, P is the variability period, ϕ is the phase shift, and t is the observation epoch. Our best-fitting value for the period of LP 705−64 is 36.315 ± 0.002 min ($f = 39.653 \pm 0.002\,{\rm d}^{-1}$), with an amplitude of1.6 ± 0.2 per cent, and the best-fitting period for J1430

is 86.394 ± 0.008 min ($f = 16.668 \pm 0.002\,\mathrm{d}^{-1}$), with an amplitude of$9.8 \pm 0.8$ per cent.

Emulating our process of creating binned spectra for SDSS J1252−0234 in Reding et al. (2020), we folded our individual spectra of LP 705−64 and J1430 into eight equally spaced phase bins, each covering one-eighth of the respective variability periods. We then averaged the exposures within each bin into composite spectra. Our selected exposure time for the LP 705−64 set provided perfect temporal alignment of spectra within each bin, allowing for simple averaging, while for J1430 we accounted for blending across phase bins by weighting spectra during rebinning according to the fraction of the acquisition time spanning each bin.

The brightnesses of our objects and relatively long exposure times made the Zeeman-split Balmer features visible even in single spectra. For LP 705−64, the folded time-series spectroscopy revealed two distinct emission phases presenting different magnetic field strengths, but which were unexpectedly separated by four ∼9-min acquisitions, i.e. one *TESS* period separated the two emission phases, rather than reflecting a full variability cycle. This suggests that a half rotation, rather than a full rotation, is occurring on this time-scale. The true rotation period of LP 705−64 must therefore be twice that of the *TESS* signal at $P_{\mathrm{LP705-64}} = 72.629 \pm 0.004$ min; we have adopted this convention throughout. Our other target, J1430, returned to its original orientation on the same period as the *TESS* signal, so we infer its rotation period to be $P_{\mathrm{LP705-64}} = 86.394 \pm 0.008$ min.

Past DAHe discoveries all present maximal emission at photometric minimum, and LP 705−64 and J1430 appear to follow this same trend by visual inspection of the slopes of spectral continua – the emission phases are present when the continua have the flattest slopes. However, for both of our objects, these slopes eventually become unreliable due to encroaching clouds in the final few exposures. Consequently, we do not attempt to convolve our binned spectra of LP 705−64 and J1430 with theoretical filter profiles to obtain rough 'light curves' of our acquisitions, as we did for SDSS J1252−0234 in Reding et al. (2020). We also did not select acquisition times based on anticipated photometric variability phases projected from *TESS* ephemerides, as our time-series spectroscopy was too far separated in time from the *TESS* photometry to predict times of maxima or minima with sufficient accuracy. Instead, our division of the variability periods into eight bins provides enough temporal resolution to select spectral phases close to expected photometric maxima and minima.

For LP 705−64, the maximum magnetic field strength visible in the top panels of Fig. 3 occurs at a phase within 5 per cent of the photometric minimum of the *TESS* observations. The maximum field strength (emission phase) for J1430 also occurs significantly closer to the *TESS* photometric minimum than the weaker magnetic absorption phase. However, extrapolating the ephemeris uncertainties forward to our spectral acquisition times produces error bars on these associations that span nearly a full variability cycle. We therefore invite additional photometric observations that can better reveal the light curve morphology and confidently associate the notable spectral phases with maxima and minima.

3.2 Magnetic field strengths

To determine magnetic field strengths, we performed least-squares fits of the H α and H β profiles at maximum emission and absorption phases using the PYTHON package LMFIT (Newville et al. 2014). We used a Lorentzian profile for wide absorption features, where applicable, and Gaussian profiles for individual Zeeman components. After finding centroid locations of the feature components, we converted these into magnetic field strength estimates using the magnetic transitions catalogued in Schimeczek & Wunner (2014). Unlike previously analysed DAHe, both LP 705−64 and J1430 host magnetic fields that evolve significantly across their rotational periods (Fig. 3).

For LP 705−64, H α and H β manifest as Zeeman-split emission with no underlying absorption in both notable spectral phases. In the narrower triplet emission phase, both features are consistent with a field strength of $B = 9.4 \pm 0.6$ MG, before they disappear into the continuum and reappear as significantly wider Zeeman emission corresponding to a field strength of $B = 22.2 \pm 0.9$ MG. These values represent the weighted averages of the individual field strength estimates from each Zeeman component, with weights determined by respective uncertainties. The overall uncertainty on the weighted average is the standard deviation of the maximally dispersed component estimates.

J1430 mimics SDSS J1252−0234 in exhibiting H β absorption at apparent photometric maximum and emission at photometric minimum. However, unlike its predecessor, in J1430 this absorption is Zeeman-split with a magnetic field strength of $B = 5.8 \pm 0.3$ MG, which becomes partially and asymmetrically filled by emission from a stronger magnetic field of $B = 8.9 \pm 1.4$ MG at the opposite phase. H α more prominently displays this emission as a fully resolved triplet, allowing for easy calculation of this field strength.

3.3 Magnetic field geometries

Reding et al. (2020) found that SDSS J1252−0234 transitions across its variability period from presenting slightly broadened, but not Zeeman-split, Balmer absorption features at photometric maximum, to revealing its significant H β Zeeman triplet emission at photometric minimum. This indicates that the magnetic spot, above which the emission manifests and displays the strongest concentration of magnetic field lines, is oriented along our line of sight at photometric minimum. This orientation consequently provides the best measure of the polar magnetic field, while the absorption centre in the opposite phase returns closer to the rest-frame wavelength of H β. This evolution of the apparent magnetic influence on Balmer features with stellar rotation illustrates that we observe different hemisphere-averaged magnetic fields across the variability phases.

J1430 behaves similarly in transitioning from absorption to emission with an apparent growing magnetic field strength, but differs in its strongly Zeeman-split absorption phase. Furthermore, the J1430 emission phase does not seem to show a clean single-field feature as was seen in SDSS J1252−0234; rather, the previous Zeeman absorption seems to still be present and asymetrically filled, possibly indicating a superposition of two apparent magnetic field signatures. H α, conversely, does not show as complicated a transition, with its emission phase presenting an easily measurable feature corresponding to a single field.

LP 705−64 adds further complexity in magnetic field presentation by never showing absorption, but instead exhibiting two emission phases corresponding to drastically different magnetic field strengths at its photometric minima. These two new discoveries therefore break the previous DAHe mold by presenting multiple distinct magnetic field signatures, while the previous three members only displayed Zeeman splitting corresponding to single field strengths. However, as with other known magnetic white dwarfs (e.g. Martin & Wickramasinghe 1984), it is often difficult to distinguish offset dipole emission from higher-order field geometries.

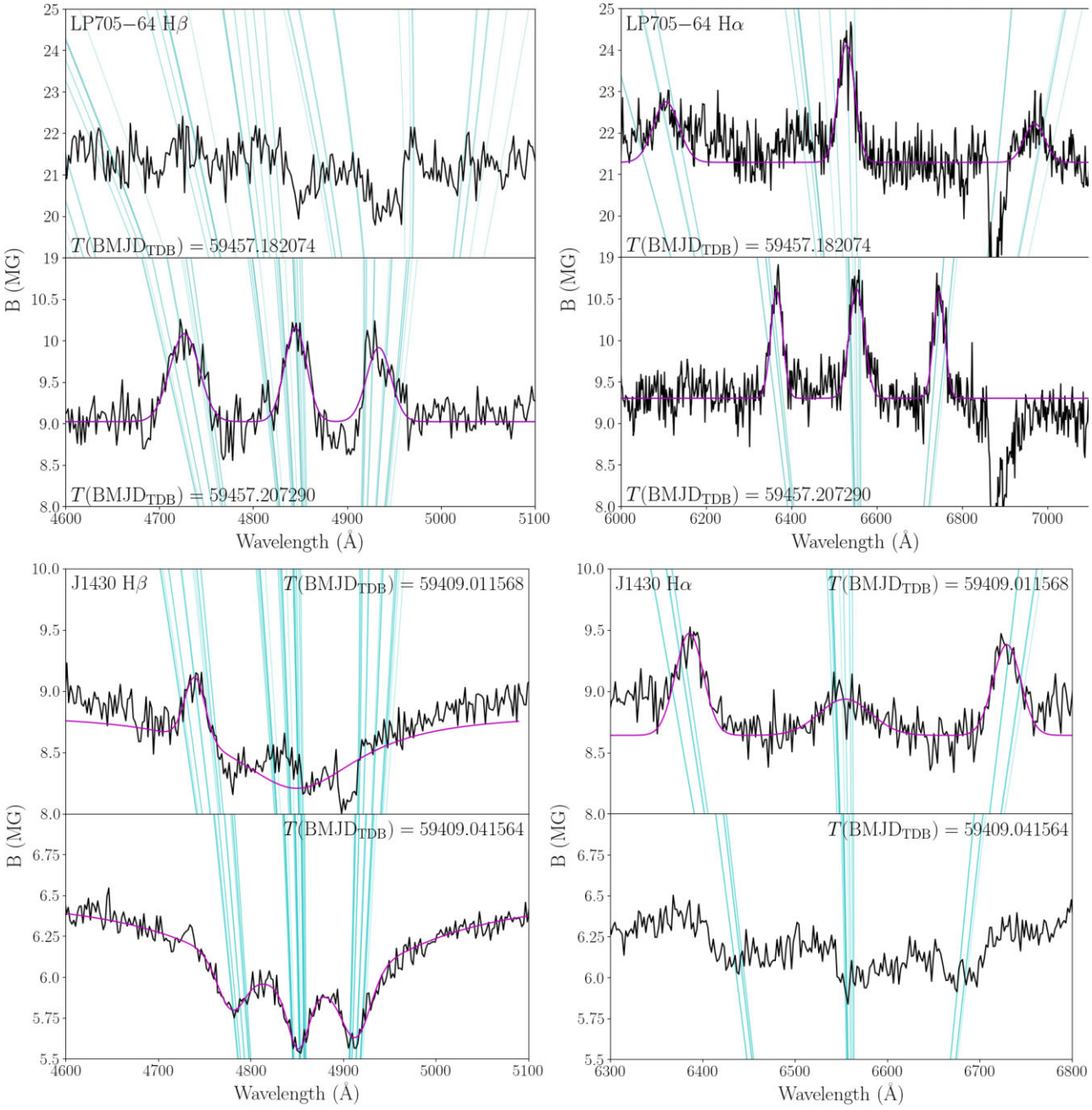

Figure 3. Hβ and Hα profiles of LP 705−64 and J1430 from binned SOAR spectra at maximum emission and absorption phases. We determine feature locations from least-squares fitting where possible, and report corresponding magnetic field strengths in Table 2. The absorption feature at ∼6900 Å in the Hα spectra of LP 705−64 (b) is telluric, which partially obscures the σ_+ Zeeman component in the wide emission phase. Given the uncertainty in projecting the *TESS* ephemerides forward to our spectral acquisition times, we instead present the mid-points of the binned spectra in BMJD$_{\rm TDB}$ as markers for future analysis. The data behind this figure are available in the article's online supplementary material.

3.4 Companion limits

Owing to their small sizes, the only potential binary systems that can fit within non-overluminous apparently isolated white dwarf spectral energy distributions are double degenerate systems containing at least one white dwarf of very high mass, or substellar companions which emit most strongly in infrared wavebands. The former case invokes a super-Chandrasekhar-mass binary system, which has never been observed even in targeted searches for the most extreme supernova Ia progenitors (Rebassa-Mansergas et al. 2019). We disregard this for LP 705−64 and J1430 given the lack of substantial radial velocity variability, and only assess potential substellar companions.

The *Wide-field Infrared Survey Explorer* (*WISE*; Wright et al. 2010) collected infrared photometry of both LP 705−64 (WISE J003513.00–122510.8) and J1430 (WISE J143019.77−562357.5) in 2015, which was reported in the CatWISE2020 catalogue (Marocco et al. 2021). We use these measurements and the averaged *WISE* photometry for late-spectral-type objects from the Database of Ultracool Parallaxes (Dupuy & Liu 2012) to place limits on potential substellar companions to each white dwarf. Because the peak

Table 2. LP 705−64 and J1430 magnetic field strengths as measured from H α and H β at notable spectral phases (Fig. 3). Field strength estimates are derived from least-squares Gaussian profile component fits and magnetic transitions calculated in Schimeczek & Wunner (2014).

Object	Phase	T (BMJD$_{\rm TDB}$)	B (MG), H β	B (MG), H α	B (MG), Avg.
LP 705−64	Em. wide	59457.182074	–	22.2 ± 0.9	22.2 ± 0.9
	Em. narrow	59457.207290	9.3 ± 1.0	9.5 ± 0.8	9.4 ± 0.6
J1430	Emission	59409.011568	9.3 ± 0.1[a]	8.6 ± 1.4	8.9 ± 1.4
	Absorption	59409.041564	5.8 ± 0.3	–	5.8 ± 0.3

[a]This is a single measurement from σ_- as the only component fully visible in this phase. We weight the average B for this phase accordingly.

wavelengths of these substellar objects fall in the far-infrared, their fluxes typically rise when moving from the *W*1 to *W*2 bands, which runs opposite to the declining trend seen in white dwarfs whose peak wavelengths push into the ultraviolet. The *W*2 band therefore places the strongest constraints on companion spectral type. We find that *W*2 photometry of spectral type T4 exceeds the corresponding point for LP 705−64 by over 3σ, while spectral type T2 similarly exceeds the *W*2 photometry of J1430. We therefore rule out a stellar or substellar companion earlier than spectral type T.

4 DISCUSSION AND CONCLUSIONS

We present the discoveries of two new DAHe white dwarfs, LP 705−64 ($0.81 \pm 0.04\,M_\odot$, $T_{\rm eff} = 8440 \pm 200$ K) and WD J143019.29−562358.33 ($0.83 \pm 0.03\,M_\odot$, $T_{\rm eff} = 8500 \pm 170$ K), bringing the total population of the DAHe class to five objects.[1]

Using time-series spectroscopy from the 4.1-m SOAR telescope, we captured signatures of evolving magnetic fields in each star with rotational phase, setting them apart from the previously discovered members of this class which only presented Zeeman splitting corresponding to single magnetic field strengths. LP 705−64 appears to rotate at 72.629 min and displays Zeeman-split Balmer emission at two separate emission phases, corresponding to magnetic field strengths of $B = 9.4 \pm 0.6$ MG and $B = 22.2 \pm 0.9$ MG. At its weakest, J1430 presents Zeeman-split Balmer absorption corresponding to a magnetic field strength of $B = 5.8 \pm 0.3$ MG. Half an 86.394-min rotation cycle later, the absorption appears superimposed with Balmer emission corresponding to a stronger magnetic field strength of $B = 8.9 \pm 1.4$ MG. As with the previously known DAHe, the maximum magnetic field strength appears coincident with the photometric minimum from the *TESS* observations, although phasing over a many-months baseline carries uncertainty. In the case of LP 705−64 we have shown that DAHe white dwarfs can show two magnetic poles.

With five members now known, the DAHe class remains relatively homogenous in its physical characteristics, with all members having mega-gauss magnetic fields, effective temperatures 7500–8500 K, and masses slightly higher than but near the white dwarf population average of $0.62\,M_\odot$ (Genest-Beaulieu & Bergeron 2019). The nature of the mechanism driving their emission remains elusive, however, as all are apparently isolated with no detectable stellar companion. As pointed out by Walters et al. (2021), the physical similarities of known DAHe strongly suggest the variability mechanism is not extrinsic, and likely represents a phase of evolution for at least some white dwarf stars.

[1]After receipt of this paper's referee report, a preprint was posted announcing spectroscopic identification of 21 northern-hemisphere DAHe white dwarfs from the Dark Energy Spectroscopic Instrument survey (Manser et al. 2023).

Thus, the origin of DAHe white dwarfs remains a mystery. In addition to strong magnetism, most of the known DAHe rotate significantly faster than a typical white dwarf. One way to generate strong magnetism and rapid rotation in white dwarfs is via a past stellar merger, especially of two white dwarfs (Ferrario et al. 1997; Tout et al. 2008; Nordhaus et al. 2011). Double-degenerate mergers may produce more massive white dwarfs, but the merger of two low-mass white dwarfs ($\lesssim 0.4\,M_\odot$) can produce a single remnant with a mass near the white dwarf average (Dan et al. 2014). It has also been speculated that planetary engulfment may spin up white dwarfs enough to generate magnetic dynamo activity (Kawka et al. 2019; Schreiber et al. 2021).

Another indicator of a merger origin is a mismatch between expected cooling age and apparent age as inferred from kinematics. This reasoning was used to classify hot carbon-atmosphere (DQ) white dwarfs as likely merger products (Dunlap & Clemens 2015). If descended from single stars without external interactions, initial–final mass relations and cooling models suggest that the DAHe white dwarfs should have $\sim 3\,M_\odot$ progenitors and roughly 2-Gyr total ages (Cummings et al. 2018; Bédard et al. 2020). Kinematic outliers could help reveal if any DAHe are merger byproducts, though this is best performed on a population rather than a single object (Cheng et al. 2020). In this context, the relatively fast kinematics of LP 705−64 ($v_{\rm tan} = 52.89$ km s^{-1}) are interesting, although are not necessarily direct evidence of a past interaction. The other known DAHe have relatively slow kinematics, with $v_{\rm tan} \approx 5$–35 km s^{-1}. Discovery and analysis of a larger sample of DAHe will better inform the kinematic ages of this sample.

ACKNOWLEDGEMENTS

This work is based on observations obtained at the Southern Astrophysical Research (SOAR) telescope, which is a joint project of the Ministério da Ciência, Tecnologia, Inovações e Comunicações (MCTIC) do Brasil, the U.S. National Optical Astronomy Observatory (NOAO), the University of North Carolina at Chapel Hill (UNC), and Michigan State University (MSU). Support for this work was in part provided by National Aeronautics and Space Administration (NASA) *TESS* Cycle 2 Grant 80NSSC20K0592 and Cycle 4 grant 80NSSC22K0737, as well as the National Science Foundation (NSF) under grants NSF AST-2108311 and PHY-1748958. We acknowledge NOIRLab programmes SOAR2021B-007 and SOAR2022A-005, as well as excellent support from the SOAR AEON telescope operators, especially César Briceño. Some of the data presented in this paper were obtained from the Mikulski Archive for Space Telescopes (MAST). Space Telescope Science Institute (STScI) is operated by the Association of Universities for Research in Astronomy, Inc., under NASA contract NAS5-26555. Support for MAST for non-*HST* data is provided by the NASA Office

of Space Science via grant NNX13AC07G and by other grants and contracts. The *TESS* data may be obtained from the MAST archive (Observation ID: tess2020266004630-s0030-0000000136884288-0195-s). This research made use of LIGHTKURVE, a PYTHON package for *Kepler* and *TESS* data analysis (Lightkurve Collaboration 2018). This work has made use of data from the European Space Agency (ESA) mission *Gaia* (https://www.cosmos.esa.int/gaia), processed by the *Gaia* Data Processing and Analysis Consortium (DPAC, https://www.cosmos.esa.int/web/gaia/dpac/consortium). Funding for the DPAC has been provided by national institutions, in particular the institutions participating in the *Gaia* Multilateral Agreement. This work makes use of data products from the Wide-field Infrared Survey Explorer, which is a joint project of the University of California, Los Angeles, and the Jet Propulsion Laboratory/California Institute of Technology, funded by NASA. This research has made use of NASA's Astrophysics Data System. This research has made use of the VizieR catalogue access tool, CDS, Strasbourg, France. This research has made use of the SIMBAD data base, operated at CDS, Strasbourg, France (Wenger et al. 2000). This research made use of ASTROPY, a community-developed core PYTHON package for astronomy (Astropy Collaboration 2013, 2018). This research made use of SCIPY (Virtanen et al. 2020), NUMPY (Harris et al. 2020), MATPLOTLIB, a PYTHON library for publication quality graphics (Hunter 2007), and the IPYTHON package (Perez & Granger 2007).

DATA AVAILABILITY

The data underlying this article are available in the article and in its online supplementary material.

REFERENCES

Astropy Collaboration 2013, A&A, 558, A33
Astropy Collaboration 2018, AJ, 156, 123
Baran A. S., Koen C., 2021, Acta Astron., 71, 113
Bédard A., Bergeron P., Brassard P., Fontaine G., 2020, ApJ, 901, 93
Brinkworth C. S., Burleigh M. R., Wynn G. A., Marsh T. R., 2004, MNRAS, 348, L33
Cheng S., Cummings J. D., Ménard B., Toonen S., 2020, ApJ, 891, 160
Clemens J. C., Crain J. A., Anderson R., 2004, in Moorwood A. F. M., Iye M.eds, Proc. SPIE Conf. Ser. Vol. 5492, Ground-Based Instrumentation for Astronomy. SPIE, Bellingham, p. 331,
Cummings J. D., Kalirai J. S., Tremblay P. E., Ramirez-Ruiz E., Choi J., 2018, ApJ, 866, 21
Dan M., Rosswog S., Brüggen M., Podsiadlowski P., 2014, MNRAS, 438, 14
Dunlap B. H., Clemens J. C., 2015, in Dufour P., Bergeron P., Fontaine G.eds, ASP Conf. Ser. Vol. 493, 19th European Workshop on White Dwarfs. Astron. Soc. Pac, San Francisco, p. 547
Dupuy T. J., Liu M. C., 2012, ApJS, 201, 19
Ferrario L., Vennes S., Wickramasinghe D. T., Bailey J. A., Christian D. J., 1997, MNRAS, 292, 205
Gänsicke B. T., Rodríguez-Gil P., Gentile Fusillo N. P., Inight K., Schreiber M. R., Pala A. F., Tremblay P.-E., 2020, MNRAS, 499, 2564
Genest-Beaulieu C., Bergeron P., 2019, ApJ, 871, 169
Gentile Fusillo N. P. et al. 2019, MNRAS, 482, 4570
Gentile Fusillo N. P. et al., 2021, MNRAS, 508, 3877
Gentile Fusillo N. P., Tremblay P. E., Jordan S., Gänsicke B. T., Kalirai J. S., Cummings J., 2018, MNRAS, 473, 3693
Goldreich P., Lynden-Bell D., 1969, ApJ, 156, 59
Greenstein J. L., McCarthy J. K., 1985, ApJ, 289, 732
Guidry J. A. et al., 2021, ApJ, 912, 125
Hallakoun N. et al., 2018, MNRAS, 476, 933
Hardy F., Dufour P., Jordan S., 2023, MNRAS, 520, 6111
Harris C. R. et al. 2020, Nature, 585, 357
Hermes J. J. et al., 2017a, ApJS, 232, 23
Hermes J. J., Gänsicke B. T., Gentile Fusillo N. P., Raddi R., Hollands M. A., Dennihy E., Fuchs J. T., Redfield S., 2017b, MNRAS, 468, 1946
Howell S. B. et al., 2014, PASP, 126, 398
Hunter J. D., 2007, Comput. Sci. Eng., 9, 90
Kaiser B. C., Clemens J. C., Blouin S., Dufour P., Hegedus R. J., Reding J. S., Bédard A., 2021, Science, 371, 168
Kawka A., Vennes S., Ferrario L., Paunzen E., 2019, MNRAS, 482, 5201
Kowalski P. M., Saumon D., 2006, ApJ, 651, L137
Lenz P., Breger M., 2014, Astrophysics Source Code Library, record ascl:1407.009
Li J., Ferrario L., Wickramasinghe D., 1998, ApJ, 503, L151
Lightkurve Collaboration 2018, Astrophysics Source Code Library, record ascl:1812.013
Luri X. et al., 2018, A&A, 616, A9
Manser C. J. et al., 2023, MNRAS, Advance Access
Maoz D., Mazeh T., McQuillan A., 2015, MNRAS, 447, 1749
Marocco F. et al., 2021, ApJS, 253, 8
Martin B., Wickramasinghe D. T., 1984, MNRAS, 206, 407
Newville M., Stensitzki T., Allen D. B., Ingargiola A., 2014, LMFIT: Non-Linear Least-Square Minimization and Curve-Fitting for Python
Nordhaus J., Wellons S., Spiegel D. S., Metzger B. D., Blackman E. G., 2011, Proc. Natl. Acad. Sci., 108, 3135
Perez F., Granger B. E., 2007, Comput. Sci. Eng., 9, 21
Podsiadlowski P., Pringle J. E., Rees M. J., 1991, Nature, 352, 783
Rebassa-Mansergas A., Toonen S., Korol V., Torres S., 2019, MNRAS, 482, 3656
Reding J. S., Hermes J. J., Vanderbosch Z., Dennihy E., Kaiser B. C., Mace C. B., Dunlap B. H., Clemens J. C., 2020, ApJ, 894, 19
Ricker G. R. et al., 2015, J. Astron. Telesc. Instrum. Syst., 1, 014003
Schimeczek C., Wunner G., 2014, ApJS, 212, 26
Schreiber M. R., Belloni D., Gänsicke B. T., Parsons S. G., 2021, MNRAS, 506, L29
Tout C. A., Wickramasinghe D. T., Liebert J., Ferrario L., Pringle J. E., 2008, MNRAS, 387, 897
Tremblay P. E. et al., 2020, MNRAS, 497, 130
Tremblay P.-E., Bergeron P., Gianninas A., 2011, ApJ, 730, 128
Vanderbosch Z. et al., 2020, ApJ, 897, 171
Vanderburg A. et al., 2015, Nature, 526, 546
Virtanen P. et al., 2020, Nat. Methods, 17, 261
Walters N. et al., 2021, MNRAS, 503, 3743
Warner B., Robinson E. L., 1972, Nat. Phys. Sci., 239, 2
Wegg C., Phinney E. S., 2012, MNRAS, 426, 427
Wenger M. et al., 2000, A&AS, 143, 9
Wickramasinghe D. T., Farihi J., Tout C. A., Ferrario L., Stancliffe R. J., 2010, MNRAS, 404, 1984
Winget D. E., van Horn H. M., Hansen C. J., 1981, ApJ, 245, L33
Wright E. L. et al., 2010, AJ, 140, 1868

SUPPORTING INFORMATION

Supplementary data are available at *MNRAS* online.

mnras_dbf.tar.gz

Please note: Oxford University Press is not responsible for the content or functionality of any supporting materials supplied by the authors. Any queries (other than missing material) should be directed to the corresponding author for the article.

This paper has been typeset from a TEX/LATEX file prepared by the author.